Inorganica Chimica Acta 396 (2013) 92–100

Contents lists available at SciVerse ScienceDirect

Inorganica Chimica Acta

journal homepage: www.elsevier.com/locate/ica

Spectroscopic, structural and magnetic investigations of iron(II) complexes based on 1-isopropyl- and 1-isobutyl-substituted tetrazole ligands

Nader Hassan [a,1], Julia Stelzl [a], Peter Weinberger [a,*], Gabor Molnar [b], Azzedine Bousseksou [b], Frank Kubel [c], Kurt Mereiter [c], Roman Boca [d], Wolfgang Linert [a]

[a] Institute of Applied Synthetic Chemistry, Vienna University of Technology, Getreidemarkt 9/163-AC, A-1060 Vienna, Austria
[b] Laboratoire de Chimie de Coordination, LCC-CNRS UPR8241, 205 Route de Narbonne, F-31077 Toulouse, France
[c] Institute for Chemical Technologies and Analytics, Vienna University of Technology, Getreidemarkt 9/164-SC, A-1060 Vienna, Austria
[d] Institute of Inorganic Chemistry, Technology and Materials (FCHPT), Slovak University of Technology, SK 812 37 Bratislava, Slovakia

ARTICLE INFO

Article history:
Received 2 February 2012
Received in revised form 12 October 2012
Accepted 17 October 2012
Available online 26 October 2012

Keywords:
Iron(II) spin-crossover
1-Isoalkyl-tetrazole
SQUID
Variable temperature IR spectroscopy
^{57}Fe–Mößbauer spectroscopy
Variable temperature UV–Vis–NIR spectroscopy

ABSTRACT

Two partly new $[Fe(intz)_6](BF_4)_2$ complexes with $n = 3$ and 4 (*i3tz* = 1-isopropyl-1*H*-tetrazole, *i4tz* = 1-isobutyl-1*H*-tetrazole) were synthesized and characterised by X-ray powder diffraction, magnetic susceptibility measurements, vibrational, electronic and ^{57}Fe–Mößbauer spectroscopy as well as DSC. The $[Fe(i3tz)_6](BF_4)_2$ complex was re-investigated and shows an incomplete spin transition at $T_c \sim 109$ K, while the $[Fe(i4tz)_6](BF_4)_2$ features a complete but rather gradual spin transition with $T_{½} = 223$ K. In the lack of suitable crystals of $[Fe(intz)_6](BF_4)_2$ with $n = 3$ and 4, we synthesized crystals of $[Ni(intz)_6](BF_4)_2$ with $n = 3$ and 4, determined their X-ray crystal structures, and proved them to be homeotypic with the respective Fe-complexes by X-ray powder diffraction. DSC measurements showed an endothermic peak for the $[Fe(i3tz)_6](BF_4)_2$ around $T = 260$ K not corresponding to a spin transition and suggesting a structural phase transition at this temperature. A well-developed peak at $T_p = 225$ K matches the spin-transition temperature $T_{½} = 223$ K for $[Fe(i4tz)_6](BF_4)_2$.

1. Introduction

One of the most fascinating molecular compounds showing bistability are iron(II) spin crossover complexes in solid state as well as in solution [1]. The potentially interesting magnetic materials need to exhibit bistability between two (or more) different spin states. The spin crossover phenomenon can be triggered by a change in temperature, pressure or irradiation with light [2], the latter being the most appealing phenomenon for technical applications [3–5]. Aiming for new materials to be used in applications such as memory devices, sensors or displays a thriving research area has been growing in the last three decades [6–9], and references therein]. In the view of applicability of these new materials a rational design of the magnetic and optical properties is of utmost importance. Unfortunately, so far no straightforward structure – property relationship has been found, but many factors and their mutual interplay seem to govern the magneto-optical behaviour of these compounds. Shedding light on the influence of these factors such as the ligand itself, the geometry of coordination, the packing of the molecules in solid state and their intermolecular interactions, the anion used or even the solvent included is a difficult task and can be best achieved via a systematic approach by varying as few parameters of the system as possible. In recent years it turned out to be useful to investigate a series of rather similar iron(II) spin crossover compounds based on the extremely versatile class of 1-substituted tetrazoles as ligands for mono- and polynuclear complexes [10–15]. In line with these investigations we focus in the present paper on two 1-isoalkane substituted tetrazoles as ligands for mononuclear iron(II) complexes and compare their structural and magnetic properties. The ligand isopropyltetrazole (*i3tz*) and its complex $[Fe(i3tz)_6](BF_4)_2$ were previously synthesized and partially characterised by Franke et al. [16]. We re-investigated this complex for an in-depth characterization and compared it with its higher homologue $[Fe(i4tz)_6](BF_4)_2$ (*i4tz* = isobutyltetrazole) we prepared for the first time.

2. Experimental

2.1. General

NaN_3 (99%), triethylorthoformate (99%), glacial acetic acid (99%), isoalkylamine (>98%) and NaOH (97%) were obtained from

* Corresponding author. Tel.: +43 1 58801 163617; fax: +43 1 58801 16299.
E-mail address: weinberg@mail.zserv.tuwien.ac.at (P. Weinberger).
[1] Present address: Chemistry Department, Faculty of Science, Suez Canal University, Ismailia, Egypt.

0020-1693
http://dx.doi.org/10.1016/j.ica.2012.10.007

Aldrich. All other chemicals were standard reagent grade and used as supplied. Elemental analyses (C, H, and N) were performed by the Mikroanalytisches Laboratorium, University of Vienna, Vienna, Austria. ^{1}H NMR and ^{13}C NMR in deuterated d_1-$CDCl_3$ were measured using a Bruker 250 FS FT NMR spectrometer. Proton NMR chemical shifts are reported in *ppm* versus TMS. Electronic spectra of the undiluted powder samples have been measured using a Perkin Elmer Lambda 900 UV–Vis–NIR spectrometer equipped with a thermostable powder sample holder in diffuse reflection geometry (Praying Mantis accessory®) between 300 and 1500 nm within the temperature range of 110 K and ambient temperature. Mid-range IR spectra of the compounds were recorded as KBr-pellets within the range 4400–450 cm^{-1} using a Perkin–Elmer 16PC FTIR spectrometer. Pellets were obtained by pressing the powdered mixture of the samples in KBr *in vacuo* using a Carver 4350 L hydraulic press applying a pressure of approx. 10000 kg/cm^2 for 5 min. Far IR spectra were recorded within the range 600–200 cm^{-1} on a Perkin–Elmer System 2000 far FTIR spectrometer using polyethylene pellets. Variable temperature IR spectra have been recorded using a Graseby Specac thermostatable sample holder.

2.2. Synthesis of the ligands

The two 1-isoalkyltetrazoles were synthesized according to literature [16] with some modifications.

1-isopropyl-1H-tetrazole: 5.9 g (100 mmol) of isopropylamine, 9.75 g (160 mmol) of sodium azide and 23.71 g (160 mmol) of triethylorthoformate were dissolved in approximately 50 ml of 99.5% acetic acid and stirred at 90 °C for 24 h. After evaporating the solvent *in vacuo* 70 ml of 2n HCl were added. The resulting solution was extracted three times with 70 ml of ethyl acetate. The combined extracts were then washed with 50 ml saturated Na_2CO_3 (aq.), brine, and then dried over anhydrous Na_2SO_4. The solvent was evaporated *in vacuo* and the resulting oil was distilled in a Kugelrohr apparatus (T = 93 °C and p = 0.75 mbar) yielding a colourless oil. Final yield: 35%. ^{1}H NMR (200 MHz, *CDCl*$_3$, 25 °C): δ = 8.61 (s, 1H, H_a), 4.83 (m, J = 6.73, 1H, H_d), 1.59(d, J = 6.65, 6H, H_e) ppm. ^{13}C NMR (50 MHz, *CDCl*$_3$, 25 °C): δ = 140.67 (C_a), 52.05 (C_d), 22.62(C_e) ppm (for assignments of C atoms, see Fig. 1). IR: $\nu_{C-H(tz)}$ = 3132 cm^{-1}

1-isobutyl-1H-tetrazole: 53.17 g freshly distilled isobutylamine, 70.91 g NaN_3 and 161.54 g triethylorthoformate were dissolved in 99.5% acetic acid and stirred at 90 °C for 41 h. The solvent and excess orthoformate were evaporated. The resulting slightly yellow solid was dissolved in 2n HCl and three times extracted with ethyl acetate. The organic phase washed with saturated Na_2CO_3 (aq.), brine, and then dried over anhydrous Na_2SO_4. After evaporating the solvent *in vacuo*, the resulting yellow oil (28.75 g ≙ 32%) was distilled in a Kugelrohr apparatus (T = 100 °C and p = 0.5 mbar). NMR spectra showed that the now colourless oil still contained impurities. Hence, it was distilled again using first a Vigreux column (T = 85 °C and p = 0.3 mbar) and finally a packed column (Raschig rings) at T = 100 °C and p = 0.5 mbar. Yield: 12.61 g ≙ 14%. ^{1}H NMR (200 MHz, d^1 *CDCl*$_3$, 25 °C): δ = 8.60 (s, 1H, H_a), 4.21 (d, J = 7.04 Hz, 2H, H_b), 2.20 (m, J = 6.82 Hz, 1H, H_d), 0.89 (d, J = 6.84, 6H, H_e) ppm. ^{13}C NMR (50 MHz, d^1 *CDCl*$_3$, 25 °C): δ = 142.82 (C_a), 55.33 (C_b), 29.26 (C_d), 19.59(C_e) ppm (Fig. 1). IR: $\nu_{C-H(tz)}$ = 3131 cm^{-1}.

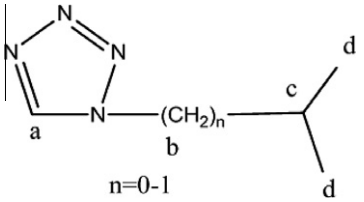

Fig. 1. Assignments of ^{13}C NMR data for the tetrazol-1-*yl*-isoalkanes.

2.3. Synthesis of the complexes

The complexes [Fe(*intz*)$_6$](BF$_4$)$_2$ with n = 3 and 4 were synthesized under argon using the Schlenk technique following the procedure given below. 0.338 g (1 mmol) $Fe(BF_4)_2{\cdot}6H_2O$ was dissolved in 5 ml ethanol, 0.672 g (6 mmol) of the 1-isopropyl-1H-tetrazole ligand (*i3tz*) and 0.757 g (6 mmol) 1-isobutyl-1H-tetrazole ligand (*i4tz*), respectively, was dissolved in 7 ml ethanol. The ligand solution was drop-wise added to the iron solution at T = 35 °C and stirred for 3 h at room temperature. After keeping the solution for 2 days at T = 4 °C diethylether was added dropwise until precipitation was complete. The white powder precipitate was filtered and dried *in vacuo*.

[Fe(*i3tz*)$_6$](BF$_4$)$_2$ (M = 902.3 g/mol, yield: 0.6 g = 0.66 mmol= 66%). Elemental *Anal.* Calc. for $C_{24}H_{48}N_{24}FeB_2F_8$: C, 32.0; H, 5.4; N, 37.3%. Found: C, 31.76; H, 5.2; N, 36.48%. IR: $\nu_{C-H(tz)}$ (300 K) = 3141 cm^{-1}; IR: $\nu_{C-H(tz)}$ (100 K) = 3132 cm^{-1}.

[Fe(*i4tz*)$_6$](BF$_4$)$_2$ (M = 986.4 g/mol; yield: 0.58 g = 0.58 mmol = 58%). Elemental *Anal.* Calc. for $C_{30}H_{60}N_{24}FeB_2F_8$: C, 36.5; H, 6.1; N, 34.1%. Found: C, 36.96; H, 6.09; N, 33.81%. IR: $\nu_{C-H(tz)}$ (300 K) = 3142 cm^{-1} IR: $\nu_{C-H(tz)}$ (100 K) = 3125 cm^{-1}.

2.4. Synthesis and single crystal X-ray diffraction of [Ni(i3tz)$_6$](BF$_4$)$_2$ and [Ni(i4tz)$_6$](BF$_4$)$_2$

After many attempts to grow single crystals of [Fe(*intz*)$_6$](BF$_4$)$_2$ suitable for X-ray structure determination had failed, we set out to overcome this problem by determining their structures via single crystals of their Ni homologues supplemented by X-ray powder diffraction of the Fe compounds, a method occasionally applied in this field [17]. For this purpose [Ni(*intz*)$_6$](BF$_4$)$_2$ with n = 3 and 4 was prepared using a 40% aqueous solution of Ni(BF$_4$)$_2$ and the appropriate molar ratios of the respective ligands in ethanolic solution. This yielded the desired good single crystals in the shape of hexagonal violet plates by slow solvent evaporation at room temperature in small crystallisation dishes.

Single crystal X-ray data of [Ni(*i3tz*)$_6$](BF$_4$)$_2$ and [Ni(*i4tz*)$_6$](BF$_4$)$_2$ were collected at T = 100 K on a Bruker Smart CCD 3-axis diffractometer using graphite-monochromated Mo Kα radiation (λ = 0.71073 Å) and ω-scan frames covering complete spheres of the reciprocal space up to θ_{max} = 30°. After data integration with program SAINT, corrections for absorption and λ/2-effects were applied with program SADABS [18]. The structures were solved with Patterson methods and were then refined on F^2 with the program package SHELX97 [19]. For non-hydrogen atoms anisotropic thermal parameters were applied and hydrogen atoms were included in idealised positions using the riding model. While [Ni(*i4tz*)$_6$](BF$_4$)$_2$ was found to have a well ordered structure, [Ni(*i3tz*)$_6$](BF$_4$)$_2$ showed an orientation disorder of the [Ni(*i3tz*)$_6$]$^{2+}$ octahedra, which, having in common a single nickel position at *x, y, z* = 0, 0, 0, adopted two significantly different orientations in a refined proportion of 0.692(2)/0.308(2). An orientation disorder of the BF_4^- anions in 0.69(2)/0.31(2) proportions was also observed. In order to improve the quality of the refinement of these features geometric restraints of the types SAME, DFIX, and DELU [20] were applied. Consistent with disorder, diffuse scattering features were seen on the recorded frames. Crystal data and experimental details are given in Table 1. Selected geometric data are presented in Table 2. Representative graphs of the two crystal structures are given in Figs. 2–4.

Many complexes [M(*alkyl-tz*)$_6$](*XY*$_4$)$_2$, where M^{2+} represents a divalent cation like Fe^{2+}, Ni^{2+}, Zn^{2+}, *alkyl* represents methyl, ethyl,

Table 1
Crystallographic data for $[Ni(intz)_6](BF_4)_2$.

	$[Ni(i3tz)_6](BF_4)_2$	$[Ni(i4tz)_6](BF_4)$
Formula	$C_{24}H_{48}B_2F_8N_{24}Ni$	$C_{30}H_{60}B_2F_8N_{24}Ni$
Formula weight	905.19	989.33
Crystal description	violet plate	violet plate
Crystal size (mm)	0.59 × 0.36 × 0.15	0.50 × 0.40 × 0.08
Crystal system	trigonal	trigonal
Space group	$R\bar{3}$ (Number 148)	$R\bar{3}$ (Number 148)
Unit cell dimensions		
a (Å)	10.8533(4)	10.8629(3)
c (Å)	31.686(3)	36.4816(16)
V (Å^3)	3232.4(3)	3728.2(2)
T (K)	100	100
Z	3	3
ρ_{calc} (g cm^{-3})	1.395	1.322
μ (mm^{-1}) (Mo Kα)	0.536	0.471
$F(000)$	1410	1554
Number of reflections measured	15112	25143
Number of reflections unique	2093	2422
Number of reflections $I > 2\sigma(I)$	1989	2119
R_{int}	0.0215	0.0319
Number of parameters/restraints	172/68	99/0
R_1 ($I > 2\sigma(I)$)[a]	0.0314	0.0366
R_1 (all data)	0.0339	0.0469
wR_2 (all data)	0.0822	0.0972
Difference in four peaks minimum and maximum (e Å^{-3})	−0.25 and 0.59	−0.56 and 0.69

Table 2
Selected bond lengths for $[Ni(intz)_6](BF_4)_2$.

	$[Ni(i3tz)_6](BF_4)$[a]	$[Ni(i4tz)_6](BF_4)$
Ni–N4	2.0918(11)	2.0871(11)
C1–N1	1.322(5)/1.300(11)	1.3301(17
C1–N4	1.296(5)/1.337(11)	1.3215(17)
N1–N2	1.347(2)/1.343(4)	1.3492(17)
N2–N3	1.288(2)/1.289(4)	1.2920(16)
N3–N4	1.362(2)/1.362(4)	1.3600(16)
N1–C2	1.482(2)/1.470(4)	1.4694(17)
B1–F1	1.401(4)	1.370(3)
B1–F2	1.421(4)	1.3826(14)

[a] Bond distances given for predominant A-/subordinate B-orientation of the $[Ni(i3tz)_6]^{2+}$ octahedra in the disordered structure of $[Ni(i3tz)_6](BF_4)_2$, see text and Fig. 4.

1-propyl, 1-butyl, cyclopropyl, or 2-haloethyl, and XY_4^- represents anions like BF_4^- and ClO_4^-, have a strong tendency to form in crystalline state hexagonal closest packed layers of large globular $[M(alkyl\text{-}tz)_6]^{2+}$ cations with XY_4^- anions located in their trigonal interstices. These trigonal or approximately trigonal layers may then be stacked in a variety of ways to form three-dimensional lattices of triclinic, monoclinic or trigonal symmetry with space group types $P\bar{1}$, $P2_1/n$, $P2_1/c$, $C2/c$, or $R\bar{3}$ [14]. The structure of $[Ni(i4tz)_6](BF_4)_2$, on practical reasons discussed ahead of $[Ni(i3tz)_6](BF_4)_2$, is a particularly nice example for this feature as it adopts a well ordered arrangement of trigonal $[Ni(i4tz)_6](BF_4)_2$ layers, stacked above each other in a cubic closest packed fashion, *i.e.* with an ...ABCABC... stacking of the layers to give a lattice of space group symmetry $R\bar{3}$. Two views of this structure demonstrating these features are shown in Fig. 2. The same type of structure is known from $[Ni(1tz)_6](ClO_4)_2$ [21], $[Fe(3tz)_6](ClO_4)_2$ [22], $[Fe(3tz)_6](BF_4)_2$ [21,22], $[Zn(3tz)_6](BF_4)_2$ [21,23–25], $[Fe(4tz)_6](BF_4)_2$ [14], and $[Ni(C_3tz)_6](BF_4)_2$ (C_3 = cyclopropyl) [26], all crystallising in space group $R\bar{3}$ with $a \approx 10.9$ Å and c between 23.7 and 37.9 Å, whereas the two Ni compounds of the present work have $R\bar{3}$ with a = 10.85–10.86 Å and c = 31.7 and 36.5 Å. A single cation–anion pair of $[Ni(i4tz)_6](BF_4)_2$ is depicted in Fig. 3 revealing three short contacts between three F atoms of the BF_4^- anion and the tetrazolic H on C1

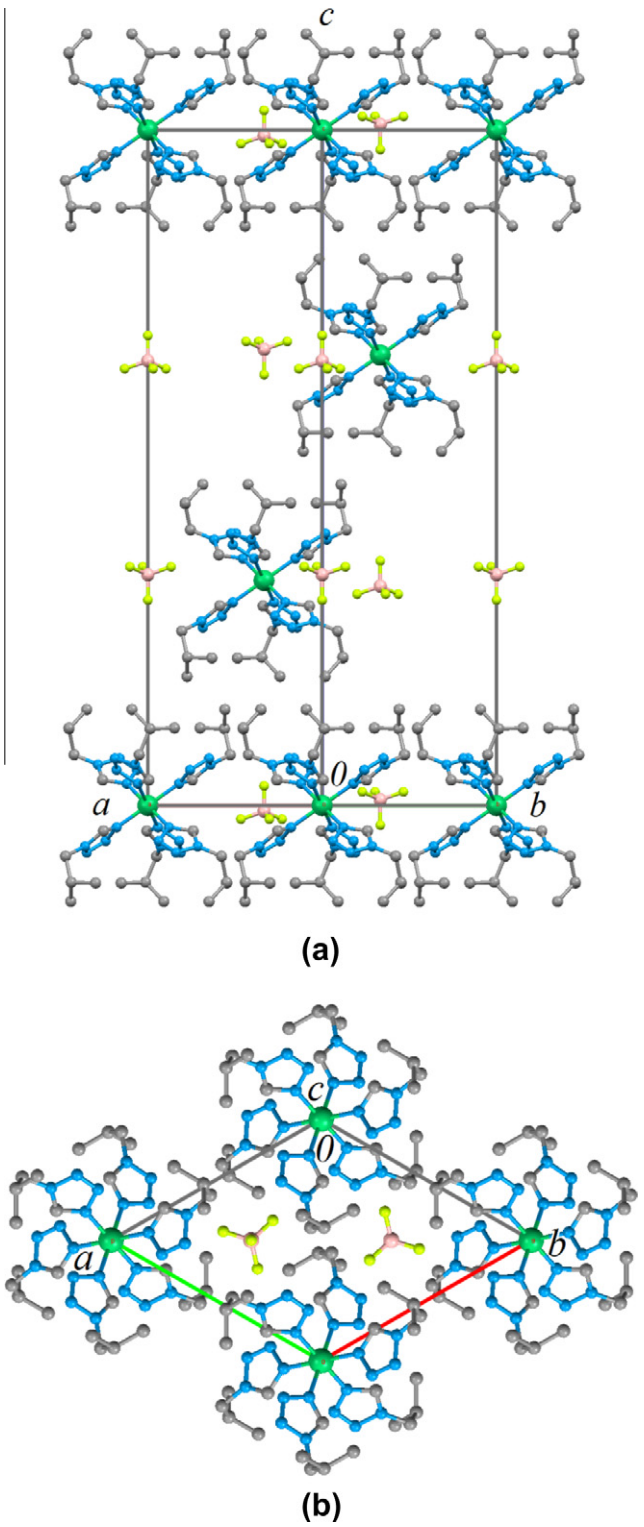

Fig. 2. Packing diagrams of $[Ni(i4tz)_6](BF_4)_2$ at 100 K. (a) View along [1 1 0], and (b) view along [0 0 1] of one $[Ni(i4tz)_6](BF_4)_2$ layer // (0 0 1) in $z \approx 0$. Ni green, N blue, C grey, B pink, and F pale green. H-atoms omitted for clarity. (For interpretation of the references to colour in this figure legend, the reader is referred to the web version of this article.)

($H(1)\cdots F(2)$ = 2.26 Å) and both α-CH_2 hydrogen atoms ($H(2b)\cdots F(1)$ = 2.48 Å and $H(2a)\cdots F(2)$ = 2.63 Å). Taking symmetry into account each BF_4^- anion is linked with its surrounding three Ni octahedra via nine C–H···F interactions, which contribute to the coherence of the structure parallel to (0 0 1). Coherence of

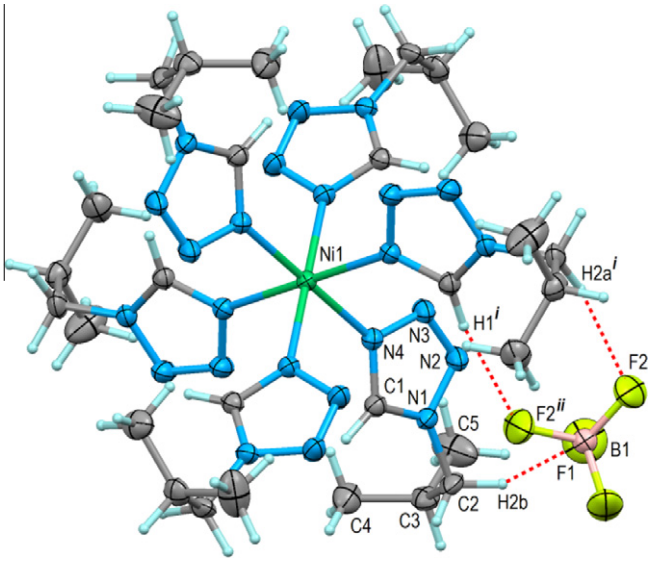

Fig. 3. Thermal ellipsoid plot (50% ellipsoids) of $[Ni(i4tz)_6](BF_4)_2$ at 100 K showing one $[Ni(i4tz)_6]^{2+}$ octahedron with hydrogen atoms and one BF_4^- anion and their C–H···F interactions (red dashed lines). View direction [001]. Only the atoms of the asymmetric unit and three symmetry equivalent ones are labelled. Symmetry codes: (i) $y, -x+y, -z$ and (ii) $1-x+y, 1-x, z$. (For interpretation of the references to colour in this figure legend, the reader is referred to the web version of this article.)

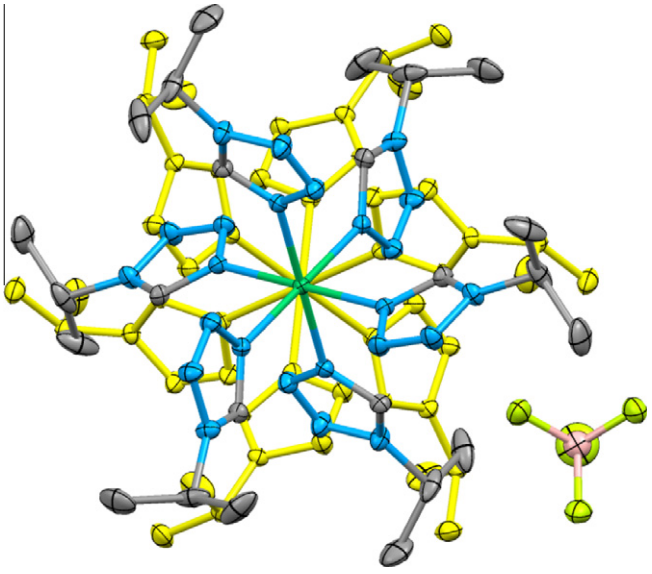

Fig. 4. Thermal ellipsoid plot (40% ellipsoids) of $[Ni(i3tz)_6](BF_4)_2$ showing the disorder in this structure, a superposition of the $[Ni(i3tz)_6]^{2+}$ octahedron in the dominant A-orientation (Ni green, N blue, C grey) and the subordinate B-orientation (all atoms yellow). H atoms and a partial orientation disorder of the BF_4 group omitted for clarity. View direction and orientation corresponds with Fig. 3. The spatial arrangement of the Ni and B atoms in the crystal lattice of $[Ni(i3tz)_6](BF_4)_2$ is the same as for $[Ni(i4tz)_6](BF_4)_2$ shown in Fig. 2. (For interpretation of the references to colour in this figure legend, the reader is referred to the web version of this article.)

the tructure perpendicular to (001) is essentially based on van-der-Waals forces with some mutual interpenetration of the structured surfaces of the $[Ni(i4tz)_6](BF_4)_2$ layers, where C(5)H$_3$ protrude most from the layers and fit into indentations above and below the Ni atoms of the adjacent layers. Despite this mutual match of layers there are two cavities of 43 Å^3 present above and below each nickel atom (at $x, y, z = 0, 0, \pm 0.12$; total solvent accessible void volume per unit cell $6 \times 43 = 258$ Å^3 per unit cell) which were found to be empty. Basically the same structure as described above is present also in $[Ni(i3tz)_6](BF_4)_2$, with the only difference that the $[Ni(i3tz)_6]^{2+}$ octahedra by disorder adopt two different orientations (A- and B-orientation) in a *ca.* 2:1 proportion, as shown in Fig. 4. Although A- and B-octahedra are similar in bond lengths and bond angles, they differ somewhat in the orientation of the tetrazole rings relative to the *c*-axis and more significantly in the orientations of the isopropyl groups relative to tetrazole moieties and to *c*-axis as well. The $[Ni(i3tz)_6]^{2+}$ octahedra in the subordinate B-orientation correspond in principle well with $[Ni(i4tz)_6](BF_4)_2$, while those in the predominant A-orientation differ from the latter (compare Figs. 3 and 4).

2.5. X-ray powder diffraction of $[Fe(i3tz)_6](BF_4)_2$ and $[Fe(i4tz)_6](BF_4)_2$

In order to verify that the two iron complexes are homeotypic with the Ni complexes (*vide supra*), X-ray powder diffraction was used. The measurements were carried out on a Panalytical X'Pert diffractometer in Bragg–Brentano geometry using Cu K$\alpha_{1,2}$ radiation, a X'Celerator linear detector with a Ni-filter, sample spinning with backloading sample holders and $2\theta = 5$–$70°$, $T = 24$ °C. Using the structural data of the Ni-complexes, Rietveld refinements were carried out with program TOPAS using the fundamental parameter approach [27]. Isotropic equivalents of the anisotropic displacement parameters of the Ni-compounds combined with an overall temperature factor were applied, but atomic coordinates were not refined. Apart from unit cell dimensions, instrumental parameters, background polynomial coefficient, a texture parameter was refined. The results are presented in Fig. 8. For $[Fe(i3tz)_6](BF_4)_2$ a very satisfying fit to the measured data was achieved with unit cell dimensions of $a = 11.0460(7)$, $c = 32.223(3)$ Å (space group $R\bar{3}$), and a texture parameter for (001) (Fig. 5a). For $[Fe(i4tz)_6](BF_4)_2$ the fit to the measured data was less satisfactory since several small residual peaks indicated the presence of an impurity. The resulting unit cell dimensions were $a = 11.983(1)$, $c = 37.662(5)$ Å (space group $R\bar{3}$), and a texture parameter for (001) (Fig. 5b). In conclusion, X-ray powder diffraction proved the homeotypism of the $[Ni(intz)_6](BF_4)_2$ and $[Fe(intz)_6](BF_4)_2$ compounds.

2.6. Magnetic susceptibility measurements

Temperature dependent magnetic susceptibility measurements were performed in an applied field of $B = 0.5$ T in a SQUID.

The magnetic susceptibility measurement for $[Fe(i4tz)_6](BF_4)_2$ reveals (see Fig. 6, left) an almost complete spin transition between $T = 170$–250 K; the estimate for the transition temperature is $T_{½} \approx 220$ K. The low-temperature tail of the magnetic susceptibility proves that some paramagnetic impurity (probably high-spin Fe(III)) is present in the sample. Different heating/cooling rates have no effect to this sample. The bulk magnetic susceptibility data have been directly fitted to the function consisting of the low-spin (LS) and high-spin (HS) fractions along with the paramagnetic impurity (PI):

$$\chi_{mol} = x_{LS}\chi_{LS} + x_{HS}\chi_{HS} + x_{PI}\chi_{PI} \quad (1)$$

using the normalisation of the mole fractions to unity: $1 = x_{LS} + x_{HS} + x_{PI}$.

Curie law has been assumed for each susceptibility contribution. With $S_{LS} = 0$, $S_{HS} = 2$ and $S_{PI} = 5/2$ ($g_{PI} = 2.0$) we are left with three free parameters: x_{PI}, g_{HS}, and eventually α_{LS} accounting to the presence of the low-lying excited state.

The temperature evolution of the high-spin mole fraction needs to be determined from an appropriate model of the spin crossover. We applied the two-level Ising-like model (equivalent to the solution model) whose essential features are well-described elsewhere

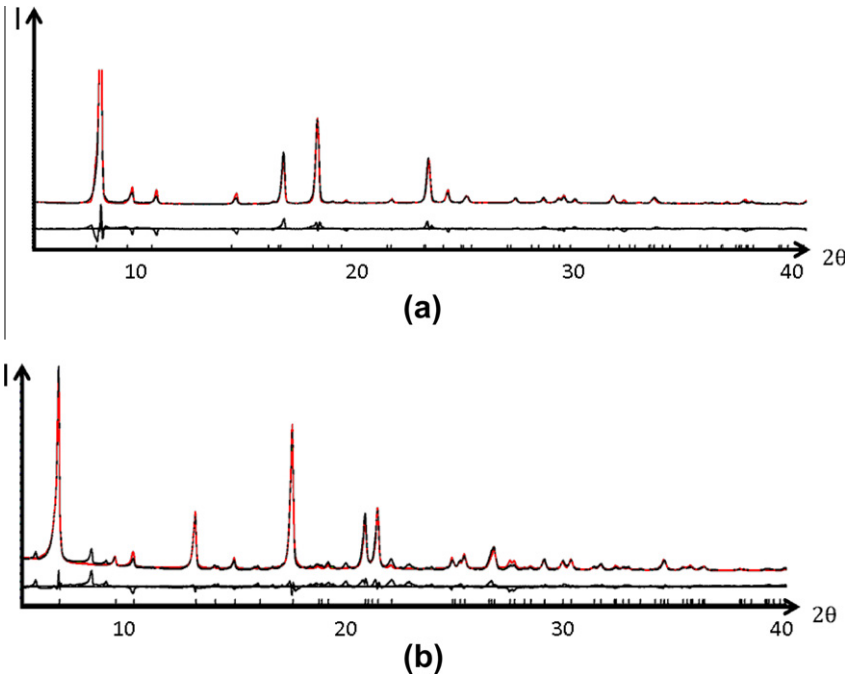

Fig. 5. Measured (black) and calculated (red) X-ray powder diffraction patterns of (a) $[Fe(i3tz)_6](BF_4)_2$ and (b) $[Fe(i4tz)_6](BF_4)_2$ at $T = 24$ °C in the range $2\theta = 5–40°$ (Cu K$\alpha_{1,2}$) with difference curves and line position tickmarks at the bottom of each graph. See text for further information. (For interpretation of the references to colour in this figure legend, the reader is referred to the web version of this article.)

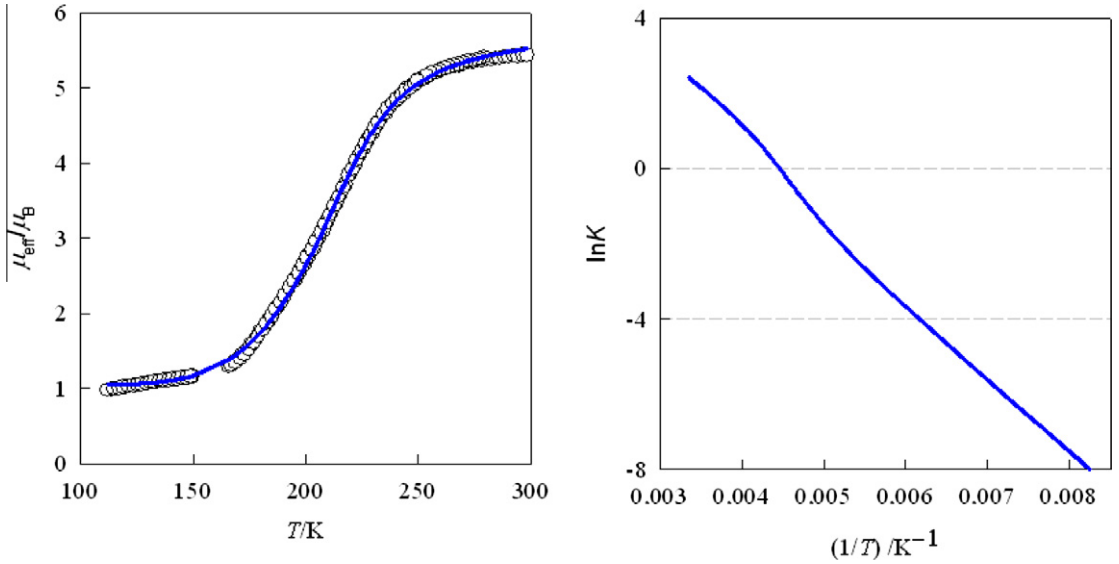

Fig. 6. Magnetic susceptibility data of the $[Fe(i4tz)_6](BF_4)_2$ (circles) and fitting the magnetic data for $[Fe(i4tz)_6](BF_4)_2$ in the heating direction; solid line – calculated; right – the van't Hoff plot.

[28]. Consequently an implicit equation is to be solved by an iterative procedure.

$$\langle\sigma\rangle = \frac{-1 + f(\langle\sigma\rangle)}{1 + f(\langle\sigma\rangle)} \tag{2}$$

where the factor

$$f = r_{eff} \exp[-(\Delta_0 - 2J\langle\sigma\rangle)/kT] \tag{3}$$

involves a thermal average of the "fictitious spin" $\langle\sigma\rangle$. The effective degeneracy ratio, $r_{eff} = d_{HS}/d_{LS} = r_{el}r_{vib} > 5$, accounts for the constant electronic as well as vibrational contributions. The positive parameter J accounts for the solid-state cooperativeness (not to be confused with the exchange coupling constant).

Inspection of Fig. 6, right reveals that the fitting procedure was successful: the calculated data (solid curve) pass through the experimental points perfectly (discrepancy factor to susceptibility is $R = 0.015$). The set of optimum parameters is: $x_{PI} = 0.027$, $\alpha_{LS} = 2.4 \times 10^{-9}$ m^3 mol^{-1}, $g_{HS} = 2.34$, $J/k = 94$ K, $\Delta_0/k = 1713$ K, and $r_{eff} = 2145$. The last two quantities gave $\Delta H = R(\Delta_0/k) = 14.2$ kJ mol^{-1} and $\Delta S = R(\ln r_{eff}) = 63.8$ J K^{-1} mol^{-1}. The transition temperature is read of for $x_{HS} = x_{LS}$ as $T_{½} = 223$ K. The solid-state cooperativeness causes a slight non-linear behaviour of the van't Hoff plot near $T_{½}$ (around ln$K = 0$).

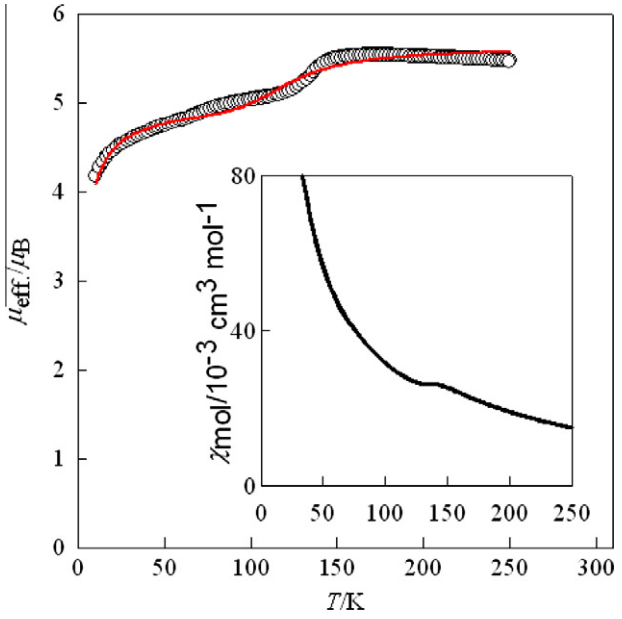

Fig. 7. Magnetic susceptibility data of the [Fe(*i3tz*)$_6$](BF$_4$)$_2$ (circles) and fitting of the magnetic data for [Fe(*i3tz*)$_6$](BF$_4$)$_2$ in the heating direction; solid line – calculated.

Also the isopropyl-species [Fe(*i3tz*)$_6$](BF$_4$)$_2$ shows a kind of spin-transition. Upon cooling the effective magnetic moment stays almost constant (μ_{eff} = 5.5 μ_B) between T = 250–150 K. At *ca.* 150 K the susceptibility displays a local maximum and on further cooling the effective magnetic moment decreases. This can be attributed to the spin crossover. However, on further cooling the susceptibility rises according to the Curie law which indicates an unconvertible iron(II) high-spin fraction that can be numerically treated like a "paramagnetic impurity" (S = 2, g_{PI} = 2.2, x_{PI} = 0.85; see Fig. 7).

2.7. ^{57}Fe–Mößbauer spectroscopy

The variable temperature ^{57}Fe–Mößbauer measurements were obtained on a constant-acceleration spectrometer with a 1.8 GBq source of ^{57}Co in a Rh-matrix. The isomer shift values (δ) are given with respect to metallic iron at room temperature. The absorber was a sample of microcrystalline powder enclosed in a 2 cm diameter cylindrical plastic holder, the size of which had been determined to optimise the absorption. The variable temperature spectra were obtained in the range of 77–300 K using a nitrogen bath cryostat (Oxford) – see Fig. 8.

Table 3
Least-squares-fitted Mößbauer data for [Fe(*intz*)$_6$](BF$_4$)$_2$.[a]

T (K)	Low spin			High spin			High-spin mole fraction x_{HS}
	δ	Δ	Γ	δ	Δ	Γ	
(a) [Fe(i3tz)$_6$](BF$_4$)$_2$							
200	0.368(4)	0.39(4)	0.150	1.107(4)	0.834(8)	0.152(6)	0.844(3)
80	0.454(2)	0.339	0.204(3)	1.166(2)	0.850(4)	0.149(3)	0.81(1)
(b) [Fe(i4tz)$_6$](BF$_4$)$_2$							
293	0.470(3)		0.129	1.022(4)	1.151(7)	0.149(2)	0.88 (2)
80	0.531(1)		0.129(2)			0	0.0

[a] δ: Isomer shift with reference to metallic iron at 293 K; Δ: quadrupole splitting; Γ: half-line width. The error bars are given in parentheses.

Fitting parameters for all spectra were obtained by using a least squares computer program (the RECOIL least-squares fitting program package under the assumption of a discrete superposition of Lorentzian lines). Least-squares-fitted Mößbauer data for [Fe(*i3tz*)$_6$](BF$_4$)$_2$ at selected temperatures are presented in Table 3. It can be seen that the Mößbauer parameters alter with temperature insignificantly. For [Fe(*i4tz*)$_6$](BF$_4$)$_2$ the small paramagnetic impurity (2.7%) is not resolved in the detected spectrum and the high-spin mole fraction match the analysis of the susceptibility data according to which x_{HS} = 0.88 at T = 293 K, and zero at T = 110 K. On the contrary, [Fe(*i3tz*)$_6$](BF$_4$)$_2$ shows only a slight decrease of the x_{HS} = 0.84 between room temperature and T = 80 K.

2.8. Variable temperature UV–Vis–NIR spectroscopy

To support the magnetic and ^{57}Fe–Mößbauer data electronic spectra have been recorded using a thermostatable solid state diffuse reflectance accessory between 110 and 300 K. The undiluted sample was measured versus a $BaSO_4$ background between 300 and 1200 nm after thermostating the sample for 10 min. According to the magnetic data of [Fe(*i3tz*)$_6$](BF$_4$)$_2$ a change of the pure HS sample is expected around 140 K upon cooling, which is reflected in the gradual raising of the typical iron(II) low-spin d–d transitions at 540 nm ($^1A_1 \rightarrow {}^1T_1$) and 380 nm ($^1A_1 \rightarrow {}^1T_2$) in the UV–Vis–NIR spectra for T = 130–110 K (see Fig. 9). As only

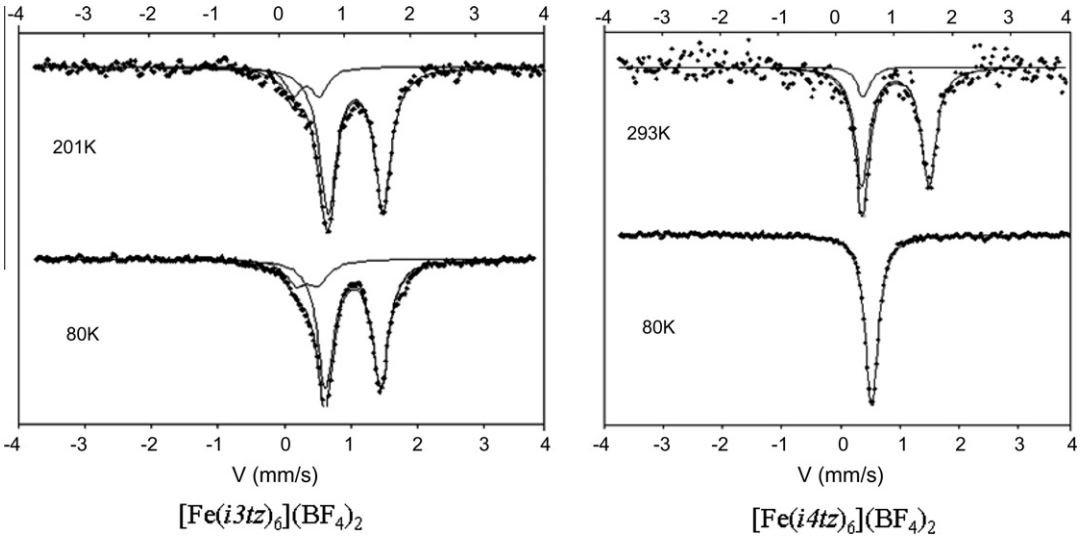

Fig. 8. ^{57}Fe–Mößbauer spectra of [Fe(*intz*)$_6$](BF$_4$)$_2$ at selected temperature (solid lines – fitted).

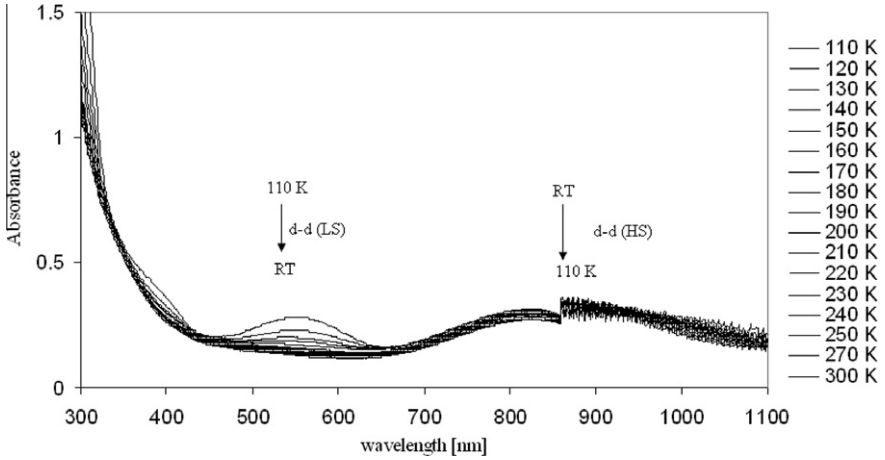

Fig. 9. Variable temperature UV–Vis–NIR spectra of $[Fe(i3tz)_6](BF_4)_2$ within $T = 110$ and 300 K.

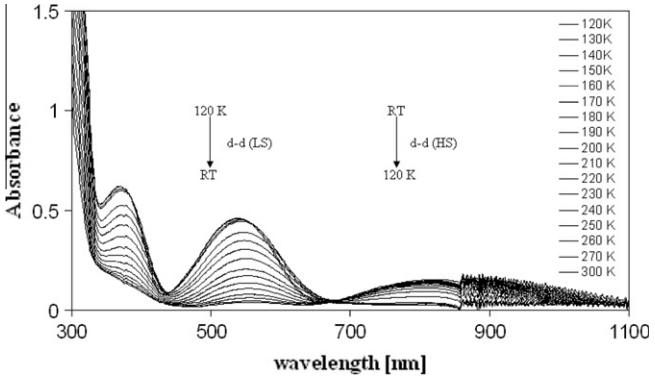

Fig. 10. Variable temperature UV–Vis–NIR spectra of $[Fe(i4tz)_6](BF_4)_2$ within $T = 120$ and 300 K.

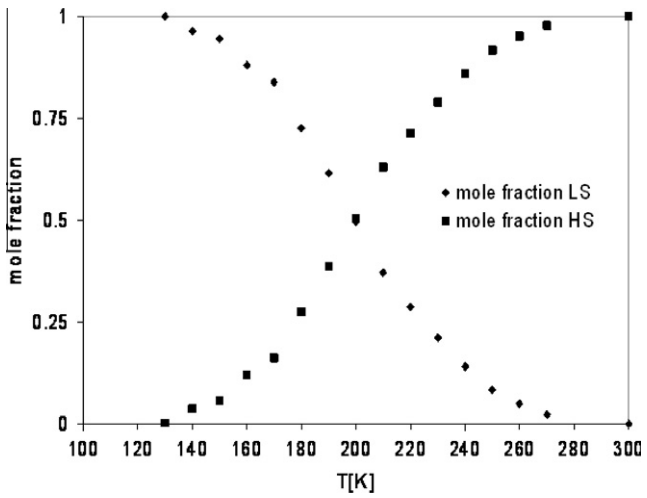

Fig. 11. Molar fractions of the LS and HS species of $[Fe(i4tz)_6](BF_4)_2$ at the respective temperatures derived from the peak areas of the d–d transition band at 540 nm.

approximately 13% of the iron(II) centres switch from high spin to low spin within the reachable temperature range of the thermostating unit of the spectrometer the dominating species at $T = 110$ K is high spin iron(II). Therefore, the intensity of the rather broad high spin iron(II) $^5T_2 \rightarrow {}^5E$ transition at 830 nm is not significantly reduced. These data match the approx. Ninety percent of iron(II) high spin derived from the ^{57}Fe–Mößbauer data at $T = 110$ K. Furthermore, the ligand field splitting energy Δ_o (LS) can be calculated according to Eq. (4) [29].

$$\Delta_o(\mathrm{LS}) = E(^1T_1) + [E(^1T_2) - E(^1T_1)]/4 \quad (4)$$

As we cannot reach a pure low spin state for the $[Fe(i3tz)_6](BF_4)_2$ at 110 K we are unable to derive the necessary spectral parameters. But Δ_o for the HS transition is obtained from the maximum of the $^5T_2 \rightarrow {}^5E$, it is equal to 11628 cm^{-1}.

According to the magnetic data of $[Fe(i4tz)_6](BF_4)_2$ a complete HS–LS transition is expected between 250 and 170 K upon cooling, which is perfectly reflected in the rather gradual raising of the typical iron(II) low-spin d–d transitions at 540 nm ($^1A_1 \rightarrow {}^1T_1$) and 380 nm ($^1A_1 \rightarrow {}^1T_2$) in the UV–Vis–NIR spectra for $T = 250$–170 K (see Fig. 10). As almost all iron(II) centres switch from high spin to low spin within the reachable temperature range of the thermostating unit of the spectrometer the only species below $T = 150$ K is low spin iron(II). Therefore, the broad high spin iron(II) $^5T_2 \rightarrow {}^5E$ transition at 830 nm is completely vanishing.

A comparison of the peak areas of the d–d band at 540 nm within the whole temperature range of the experiment allows deriving the molar fraction of the LS compound (χ_{LS}) at the respective temperature according to Eq. (5) [29]:

$$x_{LS} = \frac{A - A_0}{A_{100} - A_0} \quad (5)$$

with A_0 being the peak area at 300 K, A_{100} being the peak area at 130 K and A the peak areas at individual temperature (see Fig. 11).

As can be seen from Fig. 11 the $T_{½} \approx 200$ K can be derived from the data of the variable temperature optical spectroscopy, which represents an offset of 20 K with respect to the magnetic data (see Fig. 6). We believe that a thermostatisation problem might be the reason for this discrepancy, as we measure the temperature in the bulk powder approximately 3 mm below the surface.

Furthermore, we can determine the ligand field splitting energy Δ_o (LS) using Eq. (4) [29] (*vide supra*). Using the appropriate values for the energies the ligand field splitting energy Δ_o (LS) equals 20697 cm^{-1}. Δ_o for the HS transition is obtained from the maximum of the $^5T_2 \rightarrow {}^5E$, it is equal to 11588 cm^{-1}, which is slightly less than that of the $[Fe(i3tz)_6](BF_4)_2$.

2.9. Variable temperature Far IR spectroscopy

To monitor the change of the Fe–N bond strength change due to the spin transition variable temperature Far IR spectroscopy is an

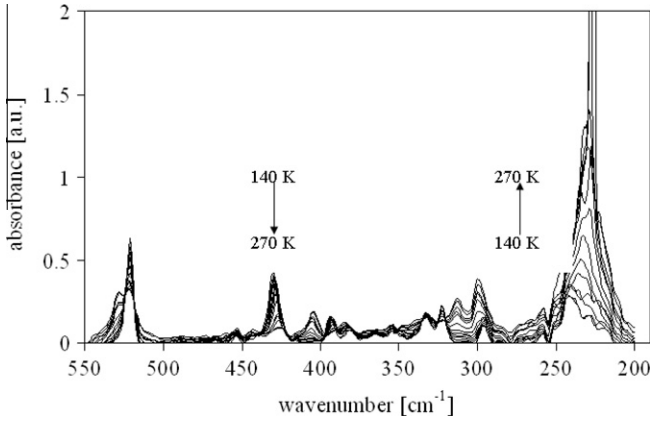

Fig. 12. Variable temperature Far IR spectra of $[Fe(i4tz)_6](BF_4)_2$ within $T = 140$ and 270 K.

ideal tool. The polyethylene pellets of the samples have been measured in a thermostatable sample holder with silicon windows in transmission between 140 and 270 K. For obtaining a reasonable signal-to-noise ratio 1000 scans have been summed up for each spectrum. The sample was thermostated 10 min for each measurement. Despite of the comparison of several molecular vibrational modes significant for the respective molecule within the measured temperature range the prominent N3–Fe–N3 mode of low spin iron(II) around 420 cm^{-1} can be used as a verification of the spin transition behaviour obtained by magnetic measurements [15]. Therefore, the Far IR spectra of $[Fe(i3tz)_6](BF_4)_2$ are monitored within the spectral range of 450–200 cm^{-1}. As within $T = 100$ and 298 K only a small percentage of the Fe(II) centres perform the spin transition, only very small changes in the spectral features can be observed.

In contrast to $[Fe(i3tz)_6](BF_4)_2$ the $[Fe(i4tz)_6](BF_4)_2$ shows a complete spin transition within $T = 140$ and 270 K, which matches the drastic spectral changes at 427 cm^{-1} representing the N3–Fe(LS)–N3 vibration and in the range between 200 and 250 cm^{-1} representing vibrational modes of the Fe(HS) (see Fig. 12).

The prominent peak at 427 cm^{-1} is used to derive molar fractions of the LS compound (χ_{LS}) at the respective temperature (refer to Eq. (1) above) given in Fig. 13 (see below). Due to the rather long measurement time (acquisition of 1000 scans for each spectrum) a good thermostatisation was achieved resulting in a perfect match of the intensity data of the typical N3–Fe(LS)–N3 peak at 427 cm^{-1} with the SQUID measurements, thus supporting the $T_{½}$ value of 220 K.

2.10. Differential scanning calorimetry (DSC)

A DSC (Perkin Elmer, Diamond; liquid-nitrogen cryogen) has been used in scanning the heat flow for several scan rates (20, 50, 100, and 200 K min^{-1}) between $T = 140$ and 290 K. As the position of the peak maximum (T_p) increases with increasing scan rate, the lowest scan rate needs to be selected for an approximate detection of the on-set of the endothermic process (see Supplementary information Figure S1). A broad endothermic peak for $n = 4$ appears in conformity with a very gradual spin crossover. The peak value T_p(DSC) = 225 K matches the value of $T_{½}$(ES) ≈ 200 K determined from electron spectroscopy, that of $T_{½}(X) \approx 225$ K from the susceptibility measurements, and $T_{½}$ (IR) = 220 K from the infrared spectra.

A weak endothermic feature at $T_p = 260$ K appears also for $n = 3$, but this is not associated with the spin transition (see Supplementary information Figure S1).

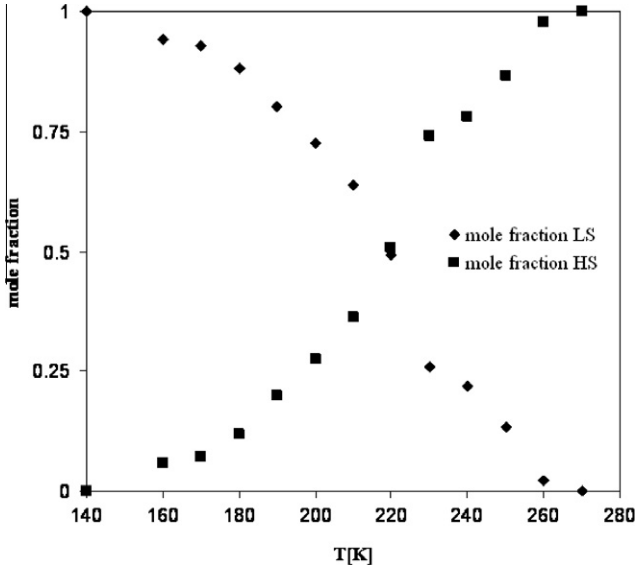

Fig. 13. Molar fraction of LS/HS of the $[Fe(i4tz)_6](BF_4)_2$ derived from the peak intensity of the N3–Fe–N3′ mode at 427 cm^{-1} yielding a $T_{½} \approx 220$ K matching the SQUID data given in Fig. 6.

3. Results and discussion

The compounds $[Fe(intz)_6](BF_4)_2$ with $n = 3$ and 4 show a surprisingly different spin transition behaviour. The not neglectable change from cyclopropyl- [30] to isopropyl-tetrazole impairs the rigidity of the terminal alkyl group and gives instead of an ordered $R\bar{3}$ structure a disordered one with the $[Fe(i3tz)_6](BF_4)_2$ octahedra in two inequivalent orientations. This feature is probably responsible for a structural phase transition at 260 K detected by DSC measurements and upon further cooling for a partial spin switching of the Fe(II) centres around $T_{SC} = 135$ K. Our finding disagrees with an early work on $[Fe(i3tz)_6](BF_4)_2$ which found no indication of a structural phase transition [31]. Insertion of just one $–CH_2–$ group right next to the tetrazole ring yielded the $[Fe(i4tz)_6](BF_4)_2$ showing a complete spin transition, although rather gradual, with a $T_{½} = 220$ K. In this case a single crystal structure of the respective Ni-homologue allows a structural insight revealing a well ordered crystal structure of $R\bar{3}$-type, which is stable for the Ni-compound down to 100 K and shows in its DSC measurements no structural phase change. In summary, this comparison of $[Fe(intz)_6](BF_4)_2$ compounds with $n = 3$ and 4 led to new insights revealing a drastic change of the spin transition behaviour depending on the existence or the length of $–CH_2–$ groups right next to the tetrazole.

Acknowledgements

Thanks for financial support are due to the "Fonds zur Förderung der Wissenschaftlichen Forschung in Österreich" (Project 19335-N17) as well as COST D35/0014/05 for granting STSM missions of Mr. Nader Hassan to Toulouse. Furthermore, we want to warmly acknowledge technical support of Lionel Rechignant (LCC/CNRS Toulouse). Grant Agencies (Slovakia: VEGA 1/0213/08, APVV 0006-07, COST-0006-06, VVCE 0004-07) are acknowledged for the financial support.

Appendix A. Supplementary material

CCDC 695383-695384 contain the supplementary crystallographic data for this paper. These data can be obtained free of

charge from The Cambridge Crystallographic Data Centre via www.ccdc.cam.ac.uk/data_request/cif.

Supplementary data associated with this article can be found, in the online version, at http://dx.doi.org/10.1016/j.ica.2012.10.007.

References

[1] W. Linert, M. Enamullah, V. Gutmann, R.F. Jameson, Monatsh. Chem. 125 (6–7) (1994) 661.
[2] B. Ordejon, C. De Graaf, C. Sousa, J. Am. Chem. Soc. 130 (2008) 13961.
[3] V.A. Money, C. Carbonera, J. Elhaik, M.A. Halcrow, J.A.K. Howard, J.F. Létard, Chem. Eur. J. 13 (2007) 5503.
[4] J.F. Létard, J. Mater. Chem. 16 (2006) 2550.
[5] B. Weber, E. Kaps, J. Weigand, C. Carbonera, J.F. Létard, K. Achterhold, F.G. Parak, Inorg. Chem. 47 (2) (2008) 478.
[6] Spin-Crossover in Transition Metal Compounds I, in: P. Gütlich, H.A. Goodwin (Eds.), Springer Verlag, 2004 ISBN 3-540-40394-9.
[7] Spin-Crossover in Transition Metal Compounds II, in: P. Gütlich, H.A. Goodwin (Eds.), Springer Verlag, 2004 3–540-40396-5.
[8] Spin-Crossover in Transition Metal Compounds III, in: P. Gütlich, H.A. Goodwin (Eds.), Springer Verlag, 2004 ISBN 3-540-40395-7.
[9] "Molecular Magnets – Recent Highlights", in: W. Linert, M. Verdaguer (Eds.), Springer Verlag, Heidelberg (Germany), 2003 ISBN 3-211-83891-0.
[10] A.F. Stassen, M. Grunert, E. Dova, M. Müller, P. Weinberger, G. Wiesinger, H. Schenk, W. Linert, J.G. Haasnoot, J. Reedijk, Eur. J. Inorg. Chem. (2003) 2273.
[11] C.M. Grunert, P. Weinberger, J. Schweifer, C. Hampel, A.F. Stassen, K. Mereiter, W. Linert, J. Mol. Struct. 733 (1-3) (2005) 41.
[12] A. Absmeier, M. Bartel, C. Carbonera, G.N.L. Jameson, P. Weinberger, A. Caneschi, K. Mereiter, J.-F. Letard, W. Linert, Eur. J. Chem. 12 (2006) 2235.
[13] M. Valtiner, H. Paulsen, P. Weinberger, W. Linert, MATCH Commun. Math. Comput. Chem. 57 (2007) 749.
[14] N. Hassan, P. Weinberger, F. Werner, K. Mereiter, G. Molnar, A. Bousseksou, M. Valtiner, W. Linert, Inorg. Chim. Acta 361 (2008) 1291.
[15] N. Hassan, P. Weinberger, F. Kubel, G. Molnar, A. Bousseksou, L. Dlhan, R. Boča, W. Linert, Inorg. Chim. Acta 362 (2009) 3629.
[16] P.L. Franke, J.G. Haasnoot, A.P. Zuur, Inorg. Chim. Acta 59 (1982) 5.
[17] A. Stassen, O. Roubeau, I. Ferrero Gramage, J. Linares, F. Varret, I. Mutikainen, U. Turpeinen, J.G. Haasnoot, J. Reedijk, Polyhedron 20 (2001) 1699.
[18] Bruker, Programs SMART, SAINT, SADABS, XPREP, and SHELXTL, Bruker AXS Inc., Madison, WI, 2001.
[19] G.M. Sheldrick, Acta Cryst. A64 (2008) 112.
[20] T. Buchen, D. Schollmeyer, P. Gütlich, Inorg. Chem. 35 (1996) 155.
[21] J. Kusz, H. Spiering, P. Gütlich, J. Appl. Crystallogr. 37 (2004) 589.
[22] L. Wiehl, Acta Crystallogr., Sect. 49 (1993) 289.
[23] M. Bokor, T. Marek, K. Suvegh, Z.S. Bocskei, J. Buschmann, A. Vertes, *Acta Phys. Pol., A* 95 (1999) 469.
[24] J.-I. Yamaura, R. Kato, Y. Nagai, H. Saito, T. Hyodo, Phys. Rev. B: Condens. Matter 58 (1998) 14098–14101.
[25] T. Marek, M. Bokor, G. Lasanda, K. Tompa, L. Parkanyi, J. Buschmann, J. Phys. Chem. Solids 61 (2000) 621.
[26] A.A. Soliman, M.M. Khattab, W. Linert, J. Coord. Chem. 58 (2005) 421.
[27] Program TOPAS, Version 4.2, Bruker AXS GmbH, Karlsruhe, Germany, 2009.
[28] R. Boča, W. Linert, Monats. Chem. 134 (2003) 199.
[29] P. Poganiuch, S. Decurtins, P. Gütlich, J. Am. Chem. Soc. 112 (1990) 3270.
[30] A. Soliman, M. Khattab, M. Reissner, P. Weinberger, F. Werner, W. Linert, Inorg. Chim. Acta 360 (2007) 3987.
[31] E.W. Müller, J. Ensling, H. Spiering, P. Gütlich, Inorg. Chem. 22 (1983) 2074.